



# Computation of the band structure of two-dimensional photonic crystals with *hp* finite elements

K. Schmidt\*, P. Kauf

Seminar for Applied Mathematics, ETH Zurich, Rämistrasse 101, 8092 Zürich, Switzerland

## ARTICLE INFO

### Article history:

Received 31 October 2007

Received in revised form 28 March 2008

Accepted 17 June 2008

Available online 2 July 2008

### Keywords:

*hp*-FEM

Exponential convergence

Corner singularities

Photonic crystals

Photonic band structure

Quasi-periodic boundary condition

## ABSTRACT

The band structure of 2D photonic crystals – a periodic material with discontinuous dielectrical properties – and their eigenmodes can be efficiently computed with the finite element method (FEM). For second order elliptic boundary value problems with piecewise analytic coefficients it is known that the solution converges extremely fast, i.e. exponentially, when using *p*-FEM for smooth and *hp*-FEM for polygonal interfaces and boundaries. In this article, we discretise the variational eigenvalue problems for photonic crystals with smooth and polygonal interfaces in scalar variables with quasi-periodic boundary conditions by means of *p*- and *hp*-FEM – this for the transverse electric (TE) and transverse magnetic (TM) modes. Our computations show exponential convergence of the numerical eigenvalues for smooth and polygonal lines of discontinuity of dielectric material properties.

© 2008 Elsevier B.V. All rights reserved.

## 1. Introduction

Photonic crystals are refractive materials with a certain periodic structure in one, two or three directions [1]. The behaviour of light in such media strongly depends on its frequency. At so called “forbidden frequencies” lying in the *band gap* of a particular photonic crystal no wave propagation is possible [2]. Such effects allow for applications in photonics and optics. For manufacturing reasons photonic crystals with two-dimensional periodicity (see Fig. 1) are very attractive.

Many properties of electrons in semiconductors, which are well explained by quantum mechanics, translate to photonic crystals. Hence, models for the description of photonic crystals are similar to those in solid state physics. For the prediction of photonic crystal properties one relies on a model of an infinite crystal with perfect periodicity. By the Floquet–Bloch transformation [3] the Maxwell eigenvalue problem for the propagating frequencies in an infinite domain is reformulated into a set of eigenvalue problems in the *elementary cell*, parameterised by the quasi-momentum  $\mathbf{k}$ . The relation between quasi-momentum and eigen frequencies is the well-known *band structure*.

There is a wide variety of methods to calculate the band structure of photonic crystals [4]. One of the most popular methods is

plane waves expansion (PWM) (see e.g. [5,6,1]), which is a Fourier series in the quasi-momentum  $\mathbf{k}$ . A pure plane waves approach experiences convergence problems for high-contrast materials, an additional smoothing of the dielectric discontinuities yields only algebraic convergence in the number of expansion coefficients [7]. Other expansion based approaches are the method of Kohn, Korringa and Rostocker (KKR) [8,9], the augmented plane waves expansion [10], which are both restricted to cylindrical structures, or the multiple multipole method (MMP) [11]. Separation of variable approaches are applied for crystals with quadratic veins [12,13]. Furthermore, there are algorithms based on finite differences in time domain (FDTD) [14–16].

Unlike the previously mentioned methods, except FDTD, the finite element method [17] uses localised basis functions defined on a mesh. Since the mesh can be unstructured and even curved, the FE method is suitable for resolving complicated geometries. In its *h*-version, i.e. the mesh width  $h$  is decreased, the numerical solutions of elliptic boundary value problems converge algebraically in the number of degrees of freedom ( $N$ ). With *p*-FEM [18,19], where we enrich the trial space with higher order basis functions, *exponential convergence* in  $N$  can be obtained, given that boundary and interfaces are smooth and the material coefficients are piecewise analytic. If, additionally, the boundary has corners, the solution is less regular, and a proper combination of mesh size  $h$  refinement and element order  $p$  enlargement, the *hp*-FEM [19,20], is needed to retain exponential convergence. This also holds for curved boundaries [21].

\* Corresponding author. Tel.: +41 44 632 60 38; fax: +41 44 632 11 04.

E-mail addresses: [kersten.schmidt@math.ethz.ch](mailto:kersten.schmidt@math.ethz.ch) (K. Schmidt), [peter.kauf@sam-math.ethz.ch](mailto:peter.kauf@sam-math.ethz.ch) (P. Kauf).

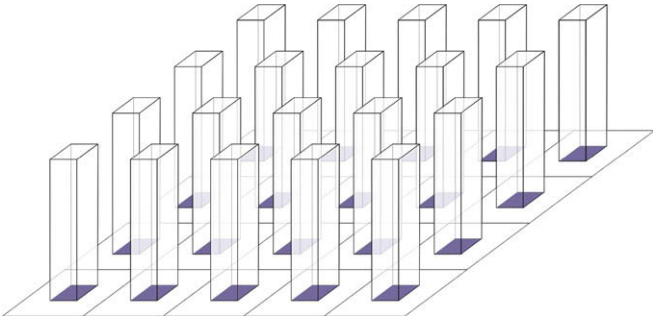


Fig. 1. A photonic crystal with two-dimensional periodicity.

For transmission problems, where there are jumping material coefficients, one expects similar convergence behaviour, especially exponential convergence

- with  $p$ -FEM for smooth interfaces,
- with  $hp$ -FEM for polygonal interfaces, if the mesh is adaptively refined to the interface corners.

These adaptively refined  $hp$ -meshes, which preserve the exponential convergence for polygonal interfaces, are created either based on *a-priori* knowledge or automatically, using *a-posteriori* error estimators. For *a priori* refinement one marks the interface corners to refine towards them.

Thereby so called *geometric meshes* occur, which, by theoretical investigations, are known to provide, together with a linearly increasing polynomial degree away from these corners, exponential convergence. *A posteriori* error estimators select cells in which the error is large – these cells are then refined or their polynomial degree is increased. Several algorithms can be found in the literature, e.g. [22,20,23], and the references therein.

Clearly, due to its exponential convergence the proposed method is asymptotically much more efficient in accuracy and computational effort than widely used FFT based methods like PWM, which converge only algebraically. Furthermore, we use trunk spaces [19], where despite of a reduction of inner degrees of freedom the approximation accuracy stays essentially the same. With these trunk spaces the constant in the exponential convergence is improved compared to the full spaces computations.

Nevertheless, to the knowledge of the authors, no paper discusses those adaptivity results for interface problems with polygonal interfaces, especially not for band structure calculations of photonic crystals. However, we refer to the recent articles on  $h$ - and  $p$ -FEM for photonic crystals in 2D [24,25] and 3D [26,27].

The objective of this article is to study the convergence of Maxwell eigenvalues of two-dimensional photonic crystals with smooth or polygonal interfaces, respectively, using *a priori* refinement strategies. We present an algorithm that computes the whole band structure quickly, because the entries of the system matrices are computed once and then changed only slightly for different  $\mathbf{k}$  values.

In chapter 2, we formulate Maxwell's equations, which decouple into two scalar problems for the transverse electric (TE) and transverse magnetic (TM) fields. Then, the periodicity in the dielectrical constant will allow us to use the Bloch transform to reformulate the eigenvalue problem on the infinite plane into a family of eigenvalue problems on the elementary cell with quasi-periodic boundary conditions. This family of problems is parametrised by the quasi-momentum  $\mathbf{k}$ . We establish weak formulations and discuss the regularity of the resulting eigenfunctions. This regularity is a criterion to choose between different strategies for designing the mesh and distributing the polynomial order to its cells.

In chapter 3, we describe the discretisation of the function spaces by  $hp$  finite elements on quadrilateral meshes with curved boundaries and with hanging nodes. First, the spaces with periodic boundaries are built. Then, we cut the basis functions into four parts, which are defined by the multiplication factors coming from the essential quasi-periodic boundary conditions. In the next step, we assemble a system matrix for each pair of these parts. The sum of these totally sixteen matrices, each multiplied by the appropriate factor, gives us the overall system matrix for one specific  $\mathbf{k}$  value.

We show numerical results in chapter 4. We compute the band structures of different geometries with curved and polygonal interfaces. A comparison to [12,13] verifies the results produced by our algorithm. In a convergence analysis we confirm the following expectations:

- The convergence of  $p$ -FEM becomes worse if there are interface corners present.
- $p$ -FEM converges only algebraically for geometries with interface corners, whereas  $hp$ -FEM recovers exponential convergence in the number of degrees of freedom.

We observe that the discretisation error for  $p$ -FEM decreases faster than for  $hp$ -FEM up to a certain number of degrees of freedom. This effect is due to the relatively moderate singularities. In these computations we use trunk spaces. We show that their convergence behaviour is better than the one using full tensor-product spaces.

## 2. Problem formulation

### 2.1. Scalar equations for TE and TM mode

In three-dimensional time-harmonic formulation of Maxwell's equations for linear, non-magnetic media, without free charges or free currents, reads

$$\operatorname{div} \mathbf{h}(\mathbf{x}) = 0, \quad \operatorname{curl} \mathbf{e}(\mathbf{x}) = -\frac{i\omega}{c} \mathbf{h}(\mathbf{x}), \quad (1a)$$

$$\operatorname{div}(\varepsilon(\mathbf{x}) \mathbf{e}(\mathbf{x})) = 0, \quad \operatorname{curl} \mathbf{h}(\mathbf{x}) = \frac{i\omega}{c} \varepsilon(\mathbf{x}) \mathbf{e}(\mathbf{x}), \quad (1b)$$

with  $\mathbf{e}(\mathbf{x})$  and  $\mathbf{h}(\mathbf{x})$  being the electric and magnetic field, respectively,  $\omega$  the angular frequency,  $c$  the vacuum speed of light,  $\varepsilon(\mathbf{x})$  the frequency-independent (relative) dielectrical constant. We assume lossless media, so  $\varepsilon(\mathbf{x})$  is real. The dielectrical constant is bounded from below by 1 and from above by a positive constant  $\varepsilon_{\max} < \infty$ .

Together with the two constraint equations and a suitable decay condition for  $|\mathbf{x}| \rightarrow \infty$ , decoupling Eq. (1) leads to two equivalent eigenvalue problems

$$\operatorname{curl} \operatorname{curl} \mathbf{e}(\mathbf{x}) = \left(\frac{\omega}{c}\right)^2 \varepsilon(\mathbf{x}) \mathbf{e}(\mathbf{x}), \quad (2a)$$

$$\operatorname{curl} \left( \frac{1}{\varepsilon(\mathbf{x})} \operatorname{curl} \mathbf{h}(\mathbf{x}) \right) = \left(\frac{\omega}{c}\right)^2 \mathbf{h}(\mathbf{x}), \quad (2b)$$

i.e. they yield the same spectrum. Since we consider the 2D case, i.e. there is only propagation in the  $(x_1, x_2)$ -plane – the plane of periodicity – but not perpendicular to it, the fields do not vary along the  $x_3$ -direction. Thus, we can split the electromagnetic fields in (2) into the transverse electric (TE) mode with  $h^1 = h^2 = e^3 = 0$  and the transverse magnetic (TM) mode with  $e^1 = e^2 = h^3 = 0$ . Each mode yields a scalar and a vector valued problem. Because both, scalar and vector valued formulations, lead to the same spectrum, it is

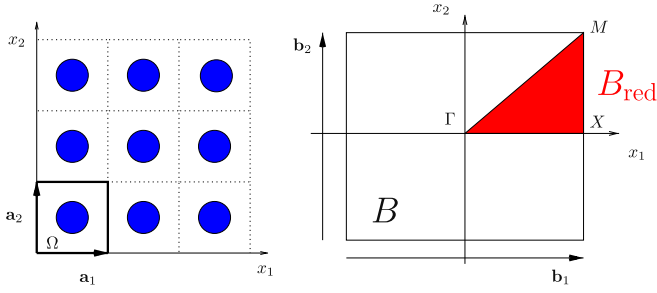


**Fig. 2.** The left picture shows a two-dimensional setting with periodicity domain  $\Omega$ . On the right side we see the corresponding Brillouin zone  $B$  and the reduced Brillouin zone  $B_{\text{red}}$  (shaded triangle).

sufficient to consider the scalar problems for TE and TM modes, which are Helmholtz like problems

$$-\text{div} \mathbf{grad} e(\mathbf{x}) = \left(\frac{\omega}{c}\right)^2 \varepsilon(\mathbf{x}) e(\mathbf{x}), \quad (3\text{-TM})$$

$$-\text{div} \left( \frac{1}{\varepsilon(\mathbf{x})} \mathbf{grad} h(\mathbf{x}) \right) = \left(\frac{\omega}{c}\right)^2 h(\mathbf{x}). \quad (3\text{-TE})$$

The eigenfunctions of (3) fulfil the Neumann transmission condition

$$[\partial_{\mathbf{n}} e(\mathbf{x})] = \left[ \frac{1}{\varepsilon(\mathbf{x})} \partial_{\mathbf{n}} h(\mathbf{x}) \right] = 0, \quad (4)$$

where  $[u]$  denotes the jump over an arbitrary, piecewise smooth Lipschitz interface  $\Gamma \subset \mathbb{R}^2$  with its unit normal vector  $\mathbf{n}$ , and  $\partial_{\mathbf{n}} u(\mathbf{x}) := \mathbf{grad} u(\mathbf{x}) \cdot \mathbf{n}$ .

## 2.2. The Bloch transformation onto the elementary cell

The photonic crystal is characterised by a periodic dielectrical constant

$$\varepsilon(\mathbf{x} + \mathbf{a}_i) = \varepsilon(\mathbf{x}), \quad i = 1, 2, \quad (5)$$

where the vectors  $\mathbf{a}_i$  are the directions of periodicity. They span the fundamental periodicity domain  $\Omega$  – a parallelogram – which is also called *elementary cell*<sup>1</sup> (see Fig. 2).

We regard  $\Omega$  as a torus, i.e. opposite sides are identified with each other. We call the geometrical sides and corners of  $\Omega$   $\Pi_i$  and  $\Gamma_i$ , respectively, with  $i \in \{1, \dots, 4\}$ , the topological sides  $\gamma_1$  and  $\gamma_2$  and the topological corner  $\pi$  (see Fig. 3).

The so called *reciprocal lattice* [28] with periodicity direction  $\mathbf{b}_1, \mathbf{b}_2$  fulfilling

$$\mathbf{a}_i \cdot \mathbf{b}_j = 2\pi \delta_{ij}, \quad i, j = 1, 2 \quad (6)$$

is associated to the photonic crystal. The elementary cell of the reciprocal lattice is the Brillouin zone<sup>2</sup>  $B$  – see Fig. 2.

Now, let us define the Floquet–Bloch transform and its inverse [3] by

$$\tilde{u}(\mathbf{k}, \mathbf{x}) = (\mathcal{F}u)(\mathbf{k}, \mathbf{x}) = \frac{1}{|B|} e^{-i\mathbf{k} \cdot \mathbf{x}} \sum_{\mathbf{m} \in \mathbb{Z}^2} u(\mathbf{x} - \mathbf{a}_{\mathbf{m}}) e^{i\mathbf{k} \cdot \mathbf{a}_{\mathbf{m}}},$$

$$u(\mathbf{x}) = (\mathcal{F}^{-1}\tilde{u})(\mathbf{x}) = \int_B e^{i\mathbf{k} \cdot \mathbf{x}} \tilde{u}(\mathbf{k}, \mathbf{x}) d\mathbf{k},$$

<sup>1</sup> Note, that the elementary cell  $\Omega$  is not uniquely defined by the vectors  $\mathbf{a}_i$ .

<sup>2</sup> The fundamental periodicity domain of the reciprocal lattice is not uniquely determined by  $\mathbf{b}_1, \mathbf{b}_2$ , so we impose the further condition that the Brillouin zone  $B$  is the set of all points belonging to a fundamental periodicity domain of the reciprocal lattice, such that  $\mathbf{k} \in B$  is closer to 0 than to any other point in the reciprocal lattice.

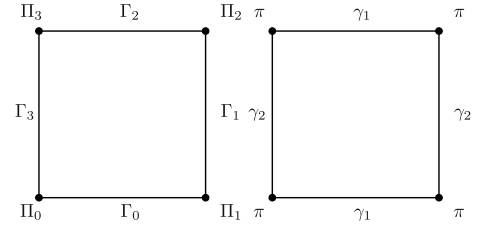


**Fig. 3.** The geometrical sides and corners (left) and the topological ones (right) of the torus  $\Omega$ .

where  $\mathbf{a}_{\mathbf{m}} = m_1 \mathbf{a}_1 + m_2 \mathbf{a}_2$ . The Floquet–Bloch transform has the same periodicity as the underlying pattern given by  $\varepsilon(\mathbf{x})$ , i.e.  $\tilde{u}(\mathbf{k}, \mathbf{x} + \mathbf{a}_i) = \tilde{u}(\mathbf{k}, \mathbf{x})$ ,  $i = 1, 2$  for all  $\mathbf{x} \in \mathbb{R}^2$ .

The Floquet–Bloch transform is an isomorphism between  $H^s(\mathbb{R}^2)$  and  $H^s(\Omega \times B)$  ( $s \in \mathbb{R}_+$ ) [3], and thus the problems (3-TM) can be transformed onto  $\Omega \times B$ , with Neumann transmission condition (4) for the jump of  $\tilde{e}(\mathbf{x})$  and  $\tilde{h}(\mathbf{x})$  over opposite sides of  $\Omega$  and modified differential operators. The whole spectrum of (2a) is the union of the spectra for all  $\mathbf{k} \in B$ . We can regard  $\mathbf{k} \in B$  as a parameter, and obtain a family of eigenvalue problems in  $\Omega$ .

However, we prefer the slightly different formulation for  $e_{\mathbf{k}}(\mathbf{x}) := e^{i\mathbf{k} \cdot \mathbf{x}} (\mathcal{F}e)(\mathbf{x}, \mathbf{k})$  and  $h_{\mathbf{k}}(\mathbf{x}) := e^{i\mathbf{k} \cdot \mathbf{x}} (\mathcal{F}h)(\mathbf{x}, \mathbf{k})$

$$-\text{div} \mathbf{grad} e_{\mathbf{k}}(\mathbf{x}) = \left(\frac{\omega}{c}\right)^2 \varepsilon(\mathbf{x}) e_{\mathbf{k}}(\mathbf{x}), \quad (7\text{-TM})$$

$$-\text{div} \left( \frac{1}{\varepsilon(\mathbf{x})} \mathbf{grad} h_{\mathbf{k}}(\mathbf{x}) \right) = \left(\frac{\omega}{c}\right)^2 h_{\mathbf{k}}(\mathbf{x}), \quad (7\text{-TE})$$

with *quasi-periodic* boundary conditions

$$e_{\mathbf{k}}(\mathbf{x} + \mathbf{a}_i) = e^{i\mathbf{k} \cdot \mathbf{a}_i} e_{\mathbf{k}}(\mathbf{x}), \quad (8a)$$

$$h_{\mathbf{k}}(\mathbf{x} + \mathbf{a}_i) = e^{i\mathbf{k} \cdot \mathbf{a}_i} h_{\mathbf{k}}(\mathbf{x}), \quad (8b)$$

and the transmission conditions

$$\partial_{\mathbf{n}} e_{\mathbf{k}}(\mathbf{x} + \mathbf{a}_i) = e^{i\mathbf{k} \cdot \mathbf{a}_i} \partial_{\mathbf{n}} e_{\mathbf{k}}(\mathbf{x}), \quad (9a)$$

$$\frac{1}{\varepsilon(\mathbf{x} + \mathbf{a}_i)} \partial_{\mathbf{n}} h_{\mathbf{k}}(\mathbf{x} + \mathbf{a}_i) = -e^{i\mathbf{k} \cdot \mathbf{a}_i} \frac{1}{\varepsilon(\mathbf{x})} \partial_{\mathbf{n}} h_{\mathbf{k}}(\mathbf{x}), \quad (9b)$$

on  $\partial\Omega$  ( $i = 1, 2$ ), with  $\mathbf{n}$  the outer normal vector on  $\partial\Omega$ .

Furthermore, if the pattern in the elementary cell has additional symmetry, e.g. mirror symmetry w.r.t. the diagonals, the so called reduced Brillouin zone  $B_{\text{red}} \subset B$  already contains the whole spectrum (see Fig. 2). A widely used fact is, that in generic cases the band gaps are located at the boundary of  $B_{\text{red}}$ , therefore the  $\mathbf{k}$ -values inside  $B_{\text{red}}$  can be neglected. In general, however, this is not true and we need the whole of  $B_{\text{red}}$  to determine the band gaps [28]. Also for the computation of other quantities such as the density of states or the Wannier functions the whole of  $B_{\text{red}}$  is needed.

## 2.3. Weak formulation

For the weak formulation of (7) we take the quasi-periodic boundary conditions (8) as essential and the transmission conditions (9) as natural boundary conditions. Thus, we define the function space

$$H_{\mathbf{k}}^1(\Omega) := \left\{ v \in H^1(\Omega) : v(\mathbf{x} + \mathbf{a}_i) = e^{i\mathbf{k} \cdot \mathbf{a}_i} v(\mathbf{x}) \text{ on } \partial\Omega, i = 1, 2 \right\},$$

and obtain: for all  $\mathbf{k} \in B_{\text{red}}$  seek pairs  $(h_{\mathbf{k}}, \omega_{\text{TE}}), (e_{\mathbf{k}}, \omega_{\text{TM}}) \in H_{\mathbf{k}}^1(\Omega) \times \mathbb{C}$ , such that  $\forall e'_{\mathbf{k}}, h'_{\mathbf{k}} \in H_{\mathbf{k}}^1(\Omega)$

$$a_{\text{TM}}(e_{\mathbf{k}}, e'_{\mathbf{k}}) = \left(\frac{\omega_{\text{TM}}}{c}\right)^2 b_{\text{TM}}(e_{\mathbf{k}}, e'_{\mathbf{k}}), \quad (10\text{-TE})$$

$$a_{\text{TE}}(h_{\mathbf{k}}, h'_{\mathbf{k}}) = \left(\frac{\omega_{\text{TE}}}{c}\right)^2 b_{\text{TE}}(h_{\mathbf{k}}, h'_{\mathbf{k}}), \quad (10\text{-TM})$$

with the inner products

$$a_{\text{TM}}(u, v) = \int_{\Omega} \mathbf{grad} u(\mathbf{x}) \cdot \overline{\mathbf{grad} v(\mathbf{x})} d\Omega, \quad (11a)$$

$$b_{\text{TM}}(u, v) = \int_{\Omega} \varepsilon(\mathbf{x}) u(\mathbf{x}) \overline{v(\mathbf{x})} d\Omega, \quad (11b)$$

$$a_{\text{TE}}(u, v) = \int_{\Omega} \frac{1}{\varepsilon(\mathbf{x})} \mathbf{grad} u(\mathbf{x}) \cdot \overline{\mathbf{grad} v(\mathbf{x})} d\Omega, \quad (11c)$$

$$b_{\text{TE}}(u, v) = \int_{\Omega} u(\mathbf{x}) \overline{v(\mathbf{x})} d\Omega, \quad (11d)$$

where  $\bar{v}$  is the complex conjugate of  $v$ .

The boundary terms from partial integration vanish due to the boundary conditions and cancellation of the factors  $e^{i\mathbf{k} \cdot \mathbf{a}_i}$  with their complex conjugates.

**Lemma 2.1.** *The eigenvalues  $\omega_{\text{TM}}$  and  $\omega_{\text{TE}}$  of (10) are real.*

**Proof 1.** Out of hermiticity in (11) it follows that all the eigenvalues  $(\frac{\omega}{c})^2 \in \mathbb{R}$ . By choosing  $e_{\mathbf{k}} = e'_{\mathbf{k}}$  and  $h_{\mathbf{k}} = h'_{\mathbf{k}}$  in Eq. (10) we also get that  $(\frac{\omega}{c})^2 \geq 0$ , implying  $\omega \in \mathbb{R}$ .

**Lemma 2.2.** *Zero eigenvalues in (10) only occur if  $\mathbf{k} = 0$ .*

**Proof 2.** We introduce the space  $H_{\mathbf{k},\infty} = H_{\mathbf{k}}^1(\Omega) \cap C^\infty(\Omega)$ , which is dense in  $H_{\mathbf{k}}^1(\Omega)$ . If  $\omega = 0$ , the only constant function in  $H_{\mathbf{k},\infty}$  is 0, but 0 is not an eigenfunction, which proves the lemma.

## 2.4. Regularity of eigenfunctions

The regularity of the eigenfunctions  $e_{\mathbf{k}}(\mathbf{x})$  or  $h_{\mathbf{k}}(\mathbf{x})$  of (7) determines the accuracy of their representation in discrete trial spaces and determines which adaptive refinement strategy is optimal.

To analyse this regularity we look at the subdomains  $\Omega_i \subset \Omega$ , in which the dielectrical constant  $\varepsilon(\mathbf{x})$  and also  $\frac{1}{\varepsilon(\mathbf{x})}$  are analytic

$$\varepsilon(\mathbf{x})|_{\Omega_i} \in \mathcal{A}(\Omega_i)$$

W.l.o.g. we assume that the elementary cell  $\Omega$  is composed into two such domains  $\Omega_1$  and  $\Omega_2$ , i.e.

$$\overline{\Omega} = \overline{\Omega_1} \cup \overline{\Omega_2}.$$

Their interface, assumed to be Lipschitz, is designated by  $\Gamma := \partial\Omega_1 \cap \partial\Omega_2$ . We consider a piecewise analytic interface  $\Gamma$ . There can be non-analytic points, i.e. there is no parametrisation around such points, for which arbitrarily high derivatives exist. We call these points *corners*, and the set of interface corners  $\mathfrak{C}$ .

### 2.4.1. Smooth interface

Let the interface be smooth, i.e.  $\mathfrak{C} = \emptyset$ . Then the eigenfunctions  $e_{\mathbf{k}}(\mathbf{x})$  or  $h_{\mathbf{k}}(\mathbf{x})$  of (7) are expected to be analytic in each subdomain up to the interface, i.e.

$$e_{\mathbf{k}}(\mathbf{x})|_{\overline{\Omega_i}} \in \mathcal{A}(\overline{\Omega_i}), \quad h_{\mathbf{k}}(\mathbf{x})|_{\overline{\Omega_i}} \in \mathcal{A}(\overline{\Omega_i}), \quad i = \{1, 2\}.$$

Just on the interface  $\Gamma$  there is a kink, but no singularity.

### 2.4.2. Polygonal interface

Now, let the interface contain corners. Then we can expect the eigenfunctions  $e_{\mathbf{k}}(\mathbf{x})$  or  $h_{\mathbf{k}}(\mathbf{x})$  to be analytic in each domain up to the interface corners  $\mathfrak{C}$ , i.e. for  $i = \{1, 2\}$

$$e_{\mathbf{k}}(\mathbf{x})|_{\overline{\Omega_i} \setminus \mathfrak{C}} \in \mathcal{A}(\overline{\Omega_i} \setminus \mathfrak{C}), \quad h_{\mathbf{k}}(\mathbf{x})|_{\overline{\Omega_i} \setminus \mathfrak{C}} \in \mathcal{A}(\overline{\Omega_i} \setminus \mathfrak{C}).$$

At the material corners  $\mathfrak{C}$  there is a singularity, i.e. there is a (higher order) derivative, which is not in  $L^2(\Omega)$ . The strength of the singularity at a corner  $\mathcal{C} \in \mathfrak{C}$  depends on the surrounding dielectrical constant and on the opening angle.

A technique to determine the singularity at  $\mathcal{C}$  for the TE mode for straight material edges is to solve a local boundary value problem<sup>3</sup>

$$-\text{div}\left(\frac{1}{\varepsilon(\mathbf{x})} \mathbf{grad} h_{\mathbf{k}}(\mathbf{x})\right) = 0$$

in polar coordinates in the neighbourhood of  $\mathcal{C}$  (see e.g. [29]). This problem has a solution of the form  $r^s(\phi)$ . A more sophisticated technique to obtain the singularity functions, based on the Kondrat'ev method, is described in [30] for the 3D case. There, the techniques used for edge singularities are applicable for the point singularities in the 2D case.

## 2.5. Mesh design principles

For smooth interfaces the eigenfunctions are piecewise analytic. In the case where the interface is exactly resolved by element boundaries, it is well known [19], that  $p$ -FEM on a fixed mesh shows exponential convergence of eigenfunctions and eigenvalues in  $N$

$$|\lambda - \lambda_N| \leq C \exp(-\beta N^{1/3}). \quad (12)$$

For polygonal interfaces the eigenfunctions are analytic up to the material corners and the singular functions are in the class of weighted spaces  $\mathcal{B}_\beta^2(\Omega)$  [31,32]. It is well known from  $hp$  theory [31,32,19], that in the case where the interface is exactly resolved by element boundaries and  $hp$  adaptive spaces are used, i.e. *a priori* the mesh is refined towards the material corners  $\mathfrak{C}$  and the polynomial degree is raised linearly away from  $\mathfrak{C}$ , the eigenfunctions are approximated with exponential convergence (12).

## 3. Algorithm

The finite elements are based on geometric meshes  $\mathcal{M}$  on the periodic domain  $\Omega$ , whose construction is explained in Section 3.1. In Section 3.2, the basis functions, which span the periodic  $hp$ -adaptive finite element space on  $\mathcal{M}$  are described. Each of these basis functions  $b(\mathbf{x})$  is cut into the four parts  $b^0(\mathbf{x}), \dots, b^3(\mathbf{x})$ . Linear combinations of these parts with phase factors define an associated quasi-periodic basis function (Section 3.3). The system matrices of the discrete eigenvalue problem for each quasi-momentum  $\mathbf{k}$  are constructed as a linear combination of phase factors and system matrices  $\mathbf{A}^m$ , which are built out of combinations of the basis function parts  $b^m(\mathbf{x})$  and  $b^n(\mathbf{x})$  (Section 3.4).

### 3.1. Geometric meshes

The periodicity cell  $\Omega$  is covered by a conforming quadrilateral mesh  $\mathcal{M}_0$  with curvilinear quadrilateral cells, that resolves the material interfaces. Thus, material corners  $\mathfrak{C}$  are cell nodes and material interfaces are represented by curved edges. Each cell is described by an element mapping  $F_K$  from the reference cell  $[0, 1]^2$ , which is constructed by Blending techniques [33].

As written in Section 2.2, we regard  $\Omega$  as a torus, i.e. opposite sides are identified with each other. To ensure this identification also for the mesh  $\mathcal{M}_0$ , opposite sides of  $\Omega$  have the same subdivision into edges and opposite edges are topologically identical, as well as all the corners of  $\Omega$  (see Fig. 3).

The *coarse mesh*  $\mathcal{M}_0$  is the root of a family of meshes  $\mathcal{M} = \{\mathcal{M}_i\}, i \in \mathbb{N}_0$ . New entities, i.e. cells, edges and vertices, accrue in  $\mathcal{M}_1$  by refining  $\mathcal{M}_0$  geometrically towards the material corners. Thus, we subdivide those cells which touch a material corner  $\mathcal{C} \in \mathfrak{C}$

<sup>3</sup> We expect the singularity to be the same for all  $\mathbf{k}$ .



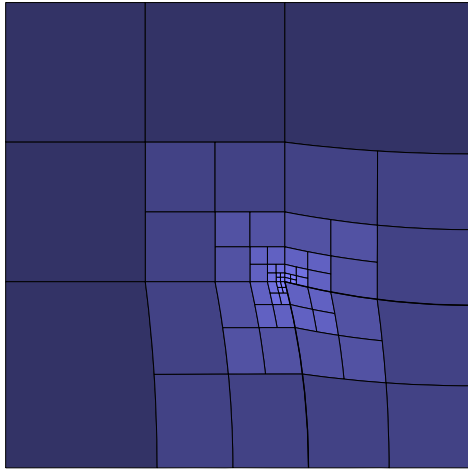


**Fig. 4.** The mesh is refined towards the interface corners, while the polynomial order increases linearly away from material corners. In this example, the mesh is two-irregular, however we can cope with arbitrarily irregular meshes.

into four cells<sup>4</sup> (see Fig. 4). The mesh  $\mathcal{M}_{i+1}$  is constructed by another subdivision of the smaller cells on  $\mathbb{C}$  in  $\mathcal{M}_i$ . The meshes  $\mathbb{M}$  that are constructed in the described way are called *geometric meshes* [19]. One could refine some cells around hanging nodes to obtain conforming meshes, however we decide to rather treat FE spaces with the up-coming non-conforming meshes than to introduce new cells (see mesh in Fig. 4).

The mesh is stored hierarchically, i.e. the cells and edges know their children. This *parent-child-relationship* permits use to decide, whether an edge or a node is hanging or not [34]. An edge is found to be hanging when itself as well as its ancestor are belonging to a lowest level cell. A node is hanging if it belongs to hanging edges only.

### 3.2. FE spaces with periodic boundary conditions

The FE space is based on elements, each consisting of a lowest level cell and shape functions, which are defined as tensor-products of polynomials on the reference element and then mapped to the cell. We use shape functions based on Jacobi polynomials [19], which are scaled integrated Legendre polynomials. They can be computed by a recursion formula for any polynomial order. Besides the full tensor-product in each cell, we heavily make use of a linearly truncated set, i.e. only internal basis functions, whose sum of the polynomial degrees in the two coordinate directions is at most  $p + 1$ , are included. For the resulting trunk spaces, also called serendipity spaces, theoretical investigations [19] predict the same convergence results for *hp*-FEM as for full tensor-product spaces on parallelogram meshes. This is easy to show for meshes with curved elements as well, since one can always find a subspace of full tensor-product elements, which shows exponential convergence as in (12). Our numerical results verify the same (see Section 4).

For a particular adaptively refined mesh  $\mathcal{M}$  we define a distribution of polynomial orders for the lowest level cells, e.g. see Fig. 4. In [34], it is described how the high order basis functions are determined for a given irregular mesh and polynomial order distribution.

Since we can cope with arbitrarily irregular meshes and arbitrary distributions of polynomial orders, we are able to use differ-

ent *a priori* and *a posteriori* refinement strategies. Nevertheless, in the present work we analysed an *a priori* refinement strategy.

**Algorithm 3.1** (*A priori hp-refinement to corners*).

- A. The regular coarse mesh – with topological identification of opposite edges – is equipped with a uniform polynomial degree  $p$ .
- B. The material corners  $\mathbb{C}$  are marked.
- C. For  $i = 1, \dots, L$  ( $L$  the number of refinements)
  - Loop over all lowest level cells  $c$  of the mesh
    - If a material corner belongs to the cell  $c$ , subdivide it. The children cells take over the polynomial degree.
    - Otherwise increase the polynomial degree of the cell  $c$ .

Algorithm 3.1 constructs a periodic space with minimal polynomial order  $p$  in the tiny cells adjacent to the marked material corners and maximal polynomial order  $p + L - 1$  or  $p + L$ , depending on whether all cells in the coarse mesh touch the material corners or not. The mesh is refined geometrically towards the material corners and becomes 1-irregular, and the polynomial degree increases linearly away from the material corners. In the next section, we explain how to construct quasi-periodic spaces and then in Section 4 we compare the eigenvalue convergence i.e. for different initial polynomial degrees.

### 3.3. FE spaces with quasi-periodic boundary conditions

Until now we have constructed the periodic *hp*-adaptive spaces  $\mathcal{S}_0^{p,1}(\Omega, \mathcal{M})$ . The basis function identified with the corner  $\pi$  of  $\Omega$  and these identified with a vertex or an edge on the sides  $\gamma_1$  or  $\gamma_2$ , will be changed to fulfil the quasi-periodic boundary conditions (8). In other words, to each periodic basis function  $b(\mathbf{x})$  we assign an appropriate quasi-periodic one,  $b^k(\mathbf{x})$  for each  $\mathbf{k}$ . For basis functions in the interior of  $\Omega$ , where  $b^k|_{\partial\Omega} = 0$ , quasi-periodic boundary conditions are trivially fulfilled, and, for all  $\mathbf{k}$  they coincide with the periodic counterpart.

In the following we derive the quasi-periodic functions  $b^k(\mathbf{x})$ . For this we additionally have to distinguish between topologically identical but geometrically different corners and sides. For notations we refer to Fig. 3.

#### 3.3.1. Definition of the quasi-periodic basis functions

First, we decompose the set of support cells  $\mathbb{K}(b)$  for each basis function  $b(\mathbf{x})$  in the periodic space  $\mathcal{S}_0^{p,1}(\Omega, \mathcal{M})$  into the four subsets<sup>5</sup>

$$\begin{aligned}\mathbb{K}_3(b) &:= \{K \in \mathbb{K}(b) : b(\bar{K} \cap \Pi_2) > 0\}, \\ \mathbb{K}_2(b) &:= \{K \in \mathbb{K}(b) : \exists \mathbf{x} \in \bar{K} \cap \Gamma_2 : b(\mathbf{x}) > 0\}, \\ \mathbb{K}_1(b) &:= \{K \in \mathbb{K}(b) : \exists \mathbf{x} \in \bar{K} \cap \Gamma_1 : b(\mathbf{x}) > 0\}, \\ \mathbb{K}_0(b) &:= \mathbb{K}(b) \setminus (\mathbb{K}_1(b) \cup \mathbb{K}_2(b) \cup \mathbb{K}_3(b)),\end{aligned}$$

and  $b(\mathbf{x})$  itself into the functions  $b^0(\mathbf{x}), \dots, b^3(\mathbf{x})$  (see Fig. 5) with

$$b^i(\mathbf{x}) := \begin{cases} b(\mathbf{x}) & \text{in } \mathbb{K}_i(b) \\ 0 & \text{otherwise.} \end{cases}$$

In Fig. 5 this decomposition is shown. A basis function identified with the (topological) corner  $\pi$  of  $\Omega$  has got four support cells, each adjacent to a corner  $\Pi_i$ , and coincides with  $\mathbb{K}_i(b)$ . Thus, the four functions  $b^i(\mathbf{x})$  represent the parts of  $b(\mathbf{x})$  belonging to one of the four support cells, respectively. A basis function identified with a

<sup>4</sup> Our code is able to refine towards edges by subdivision of neighbouring cells into two cells [34]. Resolving material edges would be interesting as well, also with anisotropic polynomial degree. This however is beyond the scope of this article.

<sup>5</sup> This is possible if the mesh has at least two cells in each direction, which we “trivially” assume from now on.

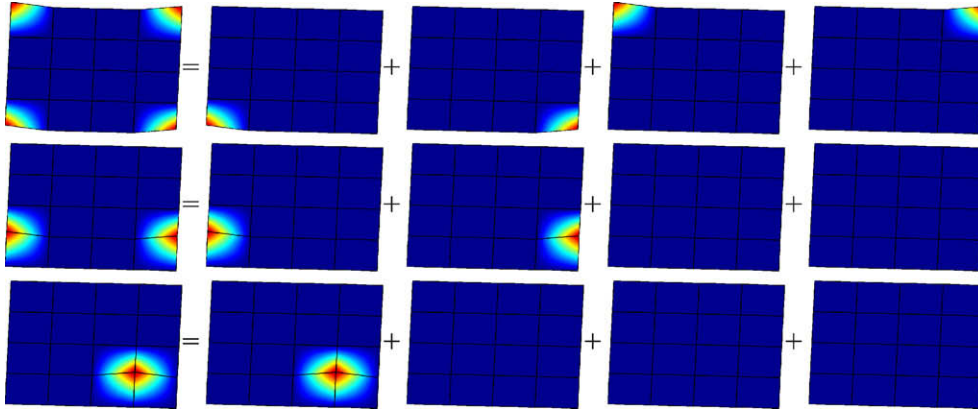


**Fig. 5.** In the *top line* we see the basis function identified with the corner  $\pi$  and its representation by functions belonging to one factor area. A basis function on the side  $\gamma_2$  is shown in the *middle line*. These basis functions are cut into two parts, whereas basis functions in the interior  $\Omega$  (bottom line) fully belong to one factor area.

(topological) side, let it be  $\gamma_2$ , has support cells<sup>6</sup> on  $\Gamma_1$  and  $\Gamma_3$ ,  $b^0(\mathbf{x})$  and  $b^1(\mathbf{x})$  are the parts of  $b(\mathbf{x})$  in these cells, respectively, the other functions  $b^2(\mathbf{x})$  and  $b^3(\mathbf{x})$  are zero. A basis function in the interior of  $\Omega$  is cut into only one piece, namely  $b^0(\mathbf{x})$ . The other functions  $b^1(\mathbf{x}), \dots, b^3(\mathbf{x})$  are zero.

Now, the functions

$$b^{\mathbf{k}}(\mathbf{x}) := b^0(\mathbf{x}) + e^{i\mathbf{k}\cdot\mathbf{a}_1} b^1(\mathbf{x}) + e^{i\mathbf{k}\cdot\mathbf{a}_2} b^2(\mathbf{x}) + e^{i\mathbf{k}\cdot(\mathbf{a}_1+\mathbf{a}_2)} b^3(\mathbf{x}),$$

meet the quasi-periodicity conditions. The span of these functions defines the space  $\mathcal{S}_{\mathbf{k}}^{\mathbf{p},1}(\Omega, \mathcal{M})$ .

With the definition of the following factors

$$\phi_{\mathbf{k}}^0 := 1, \quad \phi_{\mathbf{k}}^1 := e^{i\mathbf{k}\cdot\mathbf{a}_1}, \quad \phi_{\mathbf{k}}^2 := e^{i\mathbf{k}\cdot\mathbf{a}_2}, \quad \phi_{\mathbf{k}}^3 := e^{i\mathbf{k}\cdot(\mathbf{a}_1+\mathbf{a}_2)},$$

we can write the quasi-periodic basis functions conveniently as

$$b^{\mathbf{k}}(\mathbf{x}) := \sum_n \phi_{\mathbf{k}}^n b^n(\mathbf{x}). \quad (13)$$

### 3.3.2. Algorithmic construction of the subsets $\mathbb{K}_i$

In the following we present an algorithm to construct the subsets  $\mathbb{K}_i$ . For each cell we need to decide, whether its interior shape functions, which edge shape functions and which vertex shape functions are elements of  $\mathbb{K}_i$ . We will introduce an algorithm which is based on topological information and attribute sets only, i.e. independent of geometrical information. Vertices and edges, as well as cells are equipped with attributes, which are i.e. used for definitions of different material properties, boundary conditions or refinement strategies. By refining the mesh, these attributes are inherited by the children objects. Since opposite edges, opposite vertices and the four corners are topologically identical (see Fig. 3), they have the same attribute and we cannot decide by means of these attributes to which side of  $\Omega$  they belong. Thus, we additionally make use of cell attributes.

We need four attribute sets  $\mathcal{A}_1, \dots, \mathcal{A}_4$  for cells, two sets  $\mathcal{E}_1$  and  $\mathcal{E}_2$  for the edges and vertices on the sides of the parallelogram and  $\mathcal{P}$  for the corner<sup>7</sup>. The intersection of all these sets must be empty. In Fig. 6 there is an example of a mesh, already refined, with attribute sets  $\mathcal{A}_1 = \{1, 10\}$ ,  $\mathcal{A}_2 = \{2\}$ ,  $\mathcal{A}_3 = \{3\}$  and  $\mathcal{A}_4 = \{4\}$  for the cells,  $\mathcal{E}_1 = \{21\}$  and  $\mathcal{E}_2 = \{22\}$  for the outer edges and  $\mathcal{P} = \{30\}$  for the corners. We might have different material properties in the middle cell, therefore we assigned the additional attribute 10 to it and put

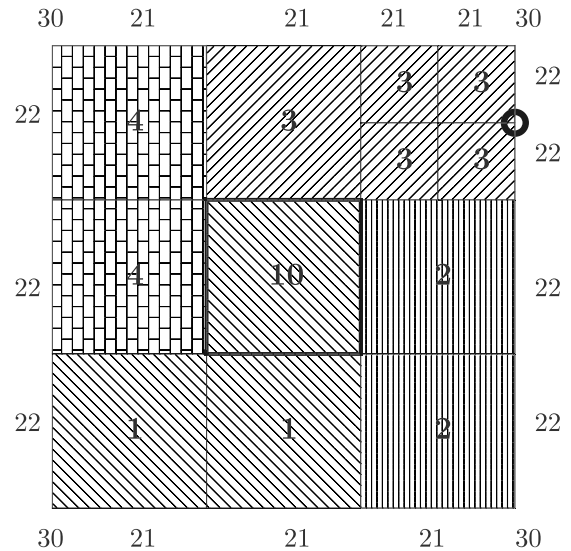


**Fig. 6.** Here, we show the necessary vertex, edge and cell attributes to determine the subsets  $\mathbb{K}_i$ . The shading of the cells corresponds to the attribute sets  $\mathcal{A}_1, \dots, \mathcal{A}_4$ . Note that the refining algorithm passes attributes from parent to child cells and edges. The middle cell gets a different dielectrical constant and so a distinct attribute.

it into  $\mathcal{A}_1$ . Furthermore, no vertex on the sides, like the marked one in Fig. 6, has an attribute.

By default all the degrees of freedom in a cell are active. To change that we use

```
CellCondition(CellAttribute,
    Tag(AttributeSet1, AttributeSet2, ...)).
```

The tags can take the values SWITCH\_OFF, SWITCH\_ON or INACTIVE. Saying SWITCH\_OFF only the degrees of freedom on the topological entities with specified attributes are inactive. SWITCH\_ON means that we activate exactly the degrees of freedom specified in the attribute list. With INACTIVE we make all the degrees of freedom within the specified cell inactive. E.g.

```
CellCondition( $\mathcal{A}_2$ , SWITCH_OFF( $\mathcal{P}, \mathcal{E}_1$ )),
```

means, that in the cells with an attribute in  $\mathcal{A}_2$  all degrees of freedom except those on the entities with attributes in  $\mathcal{P}$  or  $\mathcal{E}_1$  are built.

The subsets  $\mathbb{K}_i$  of the basis functions are determined by the following list:

<sup>6</sup> One on each side for basis functions identified with an edge, and two for those identified with a vertex.

<sup>7</sup> We have to make sure that cells which topologically share edges or vertices have different attributes.

$$\mathbb{K}_0 : \{ \text{CellCondition}(\mathcal{A}_2, \text{SWITCH\_OFF}(\mathcal{P}, \mathcal{E}_1)), \\ \text{CellCondition}(\mathcal{A}_3, \text{SWITCH\_OFF}(\mathcal{P}, \mathcal{E}_1, \mathcal{E}_2)), \\ \text{CellCondition}(\mathcal{A}_4, \text{SWITCH\_OFF}(\mathcal{P}, \mathcal{E}_1)) \},$$

$$\mathbb{K}_1 : \{ \text{CellCondition}(\mathcal{A}_4, \text{SWITCH\_ON}(\mathcal{P}, \mathcal{E}_1)), \\ \text{CellCondition}(\mathcal{A}_3, \text{SWITCH\_ON}(\mathcal{E}_1)), \\ \text{CellCondition}(\mathcal{A}_1, \mathcal{A}_2, \text{INACTIVE}) \},$$

$$\mathbb{K}_2 : \{ \text{CellCondition}(\mathcal{A}_2, \text{SWITCH\_ON}(\mathcal{P}, \mathcal{E}_2)), \\ \text{CellCondition}(\mathcal{A}_3, \text{SWITCH\_ON}(\mathcal{E}_2)), \\ \text{CellCondition}(\mathcal{A}_1, \mathcal{A}_4, \text{INACTIVE}) \},$$

$$\mathbb{K}_3 : \{ \text{CellCondition}(\mathcal{A}_3, \text{SWITCH\_ON}(\mathcal{P})), \\ \text{CellCondition}(\mathcal{A}_1, \mathcal{A}_2, \mathcal{A}_4, \text{INACTIVE}) \}.$$

Normally, most of the vertices do not have any attribute, in particular vertices created by subdivision of an edge (e.g. the vertex marked with a black circle in Fig. 6) do not have attributes. To decide if such a vertex without an attribute is located on a side of the domain, we consult the related edges, i.e. the edges to which the vertex belongs. We distinguish three cases:

- The vertex has its own attribute: it is treated according to that attribute.
- The vertex has no own attribute and only one related edge has an attribute: the vertex is treated as if it would have the attribute of that edge.
- The vertex has no own attribute and the related edges have attributes: the vertex is treated as if it would have the attribute of any one of these edges.

In the example in Fig. 6 the marked vertex is recognised to be on a vertical side, since two related edges have the attribute 22, which is contained in  $\mathcal{E}_1$ .

### 3.4. Assembly of the system matrices

For simplicity reasons we do not distinguish between TM and TE modes in this section. With the basis functions of the spaces  $\mathcal{S}_k^{p,1}(\Omega, \mathcal{M})$  defined just above, we find the matrix eigenvalue problems of (10)

$$A^k \bar{X}^k = \lambda^k M^k \bar{X}^k$$

with the system matrices

$$A^k = \left( a(b_j^k, b_j^k) \right)_{ij=1}^N, \quad M^k = \left( b(b_j^k, b_j^k) \right)_{ij=1}^N, \quad (14)$$

where  $a$  and  $b$  stand for the appropriate inner product for the TM or TE mode, respectively. The eigenvalues are  $\lambda^k = (\frac{\omega}{c})^2$ . After inserting (13) into (14) we get

$$A^k = \sum_{m,n=0}^3 \phi_k^m \phi_k^n \left( a(b_j^m, b_j^n) \right)_{ij=1}^N,$$

and with the definition of the matrices

$$A^{mn} := \left( a(b_j^m, b_j^n) \right)_{ij=1}^N,$$

we write

$$A^k = \sum_{m,n=0}^3 \phi_k^m \phi_k^n A^{mn}.$$

Due to the cutting procedure, the computation of the sixteen matrices  $A^{mn}$  is exactly as expensive as the direct computation of  $A^0$ . The multiplication with the phase factors is negligible compared to the overall cost. Thus, the assembly of an arbitrary number of the system matrices  $A^k$  for different quasi-momenta  $k \in B_{\text{red}}$  has about the same cost as the assembly of the single matrix  $A^0$ . As basis functions in the interior of  $\Omega$  are not affected by quasi-periodicity, only a small part of  $A^k$  is affected when changing  $k$ .

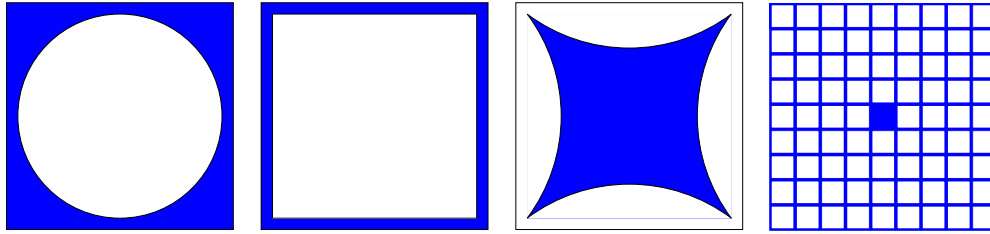


**Fig. 7.** The elementary cell with cylindrical holes (left), that with dielectric veins (inner left), that with inversely curved dielectric rods (inner right) and that with a  $9 \times 9$  structure of dielectric veins with a periodic defect in the middle (right). The white region is air ( $\varepsilon = 1$ ), the shaded region is a dielectric medium ( $\varepsilon > 1$ ).

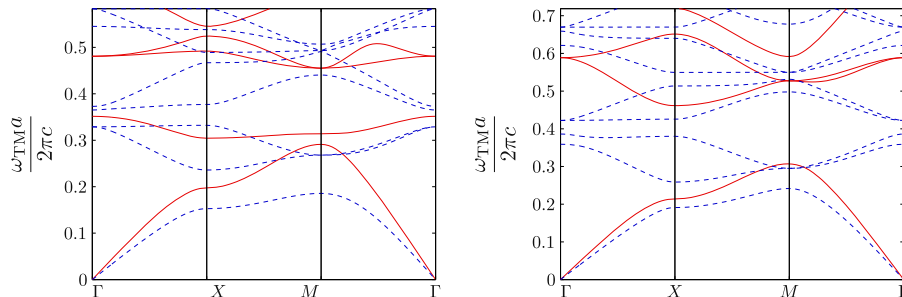


**Fig. 8.** Band structure of the crystal with cylindrical holes of diameter  $0.95a$  (left) and of the crystal with dielectric veins of thickness  $0.1a$  ( $0.05a$ ) on both sides. The dielectric medium (dark in Fig. 7) has  $\varepsilon = 20$ , in the rest of the structure we have  $\varepsilon = 1$ . Solid lines denote TE modes, dashed lines denote the TM modes.

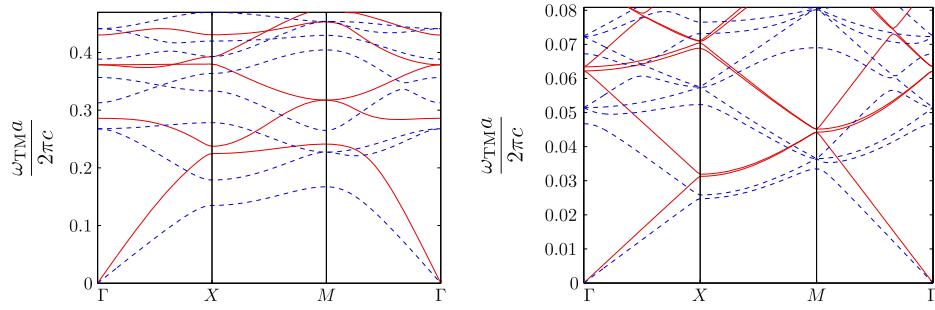


**Fig. 9.** Band structure of the crystal with inversely curved dielectric rods with radius  $0.8a$  (midpoints on the perpendicular bisectors of the sides) and distance between corners of  $0.9a$  (left) and of the crystal with a  $9 \times 9$  structure of dielectric veins of thickness  $0.1a/9$  (right). The dielectric medium (dark in Fig. 7) has  $\varepsilon = 20$ , in the rest of the structure we have  $\varepsilon = 1$ . Solid lines denote TE modes, dashed lines denote the TM modes.

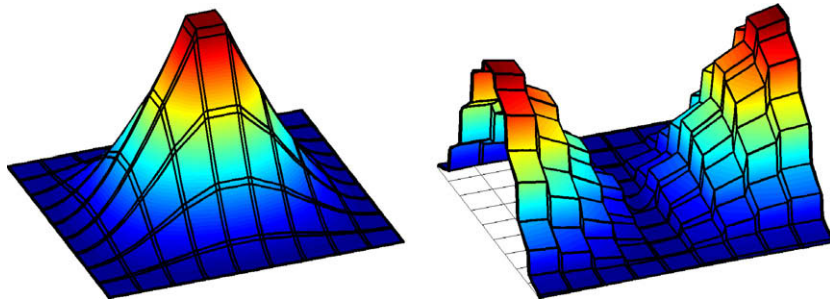


**Fig. 10.** Squared amplitude of the first TM eigenfunction  $|e_z(x)|^2$  (left) and TE eigenfunction  $|h_z(x)|^2$  (right) at the  $M$  point of the crystal with a  $9 \times 9$  structure of dielectric veins of thickness  $0.1a/9$ . The dielectric medium (dark in Fig. 7) has  $\varepsilon = 20$ , in the rest of the structure we have  $\varepsilon = 1$ . As the TE eigenvalue is twofold, there is another eigenfunction, which results from an interchange of  $x_1$  and  $x_2$ .

The integrals in (11) are computed by numerical Gauss quadrature on each element. The number of quadrature points is adapted to the maximal polynomial degree  $p = p(c)$ . We use sum factorisation [34] to reduce the integration costs from  $O(p^6)$  to  $O(p^5)$ .

#### 4. Numerical results

The band structure algorithm is implemented in our object-oriented software package Concepts [35,36], written in C++. The meshes use an exact representation of curved edges, which is needed for  $p$ -FEM and  $hp$ -FEM. In order to reduce the number of degrees of freedom  $N$ , we use trunk spaces. For  $p$ -FEM and  $hp$ -FEM we analyse the error in dependence of the number of degrees of freedom, which is essentially smaller for trunk spaces. For finding the smallest eigenvalues of the generalised matrix eigenvalue problems we use ARPACK [37], for the LU decomposition the library SuperLU [38].

##### 4.1. Band structures and eigenfunctions

We calculated the band structure of four photonic crystals defined by the pattern of their elementary cells, the cylindrical holes, the dielectric veins (both in Fig. 7), the inversely curved dielectric cylinders and a  $9 \times 9$  structure of dielectric veins with a periodic defect (both in Fig. 7).

In all cases the elementary cell is the square  $\Omega = [0, a]^2$ , which is scaled to  $\hat{\Omega} = [0, 1]^2$ , for which the Brillouin zone is  $\hat{B} = [0, 2\pi]^2$ . Then, the angular frequency  $\omega$  scales with  $1/a$ . Hence, it is convenient to look at the non-dimensional quantity  $\omega a / 2\pi c = \sqrt{\hat{\lambda}} / 2\pi$ , where  $\hat{\lambda}$  is the eigenvalue of the eigenvalue problem on  $\hat{\Omega}$ .

The computed band structures of the four photonic crystals are shown in Figs. 8 and 9. We want to emphasise that our algorithm is well suited for dielectric patterns with

- straight and curved interfaces with corners,
- structures with small local geometry features.

The refinement strategies will be discussed in Section 4.2.

**Table 1**

The table shows our results for the relative eigenvalues  $\hat{\lambda} = \omega^2 a^2 / c^2$  at the lower and upper bound of the first three bands for the dielectric veins (Fig. 7) in comparison to [12,13,24]

Band No.	TM spectrum		TE spectrum		
	Lower bound	Upper bound	Lower bound	Upper bound	
1	0	2.22	0	3.73	From [12]
	0	2.31	0	3.73	From [13]
	0	2.312	0	3.743	From [24]
	0	2.30429 (73)	0	3.719 (34)	$p$ -FEM
2	2.64	5.09	8.42	13.73	From [12]
	2.64	5.09	8.43	13.76	From [13]
	2.650	5.099	8.440	13.704	From [24]
	2.642854 (92)	5.0873131 (35)	8.40 (47)	13.678 (20)	$p$ -FEM
3	3.44	5.65	11.01	16.77	From [12]
	3.43	5.91	11.04	16.77	From [13]
	3.454	5.904	11.027	16.785	From [24]
	3.4379333 (62)	5.888 (50)	10.972 (25)	16.741 (72)	$p$ -FEM

We use a polynomial refinement strategy with nine cells and uniform polynomial order  $p = 15$  (963 degrees of freedom). The results of [24] are converted with their given accuracy.

- discontinuous dielectric constants,
- smooth, curved interfaces,



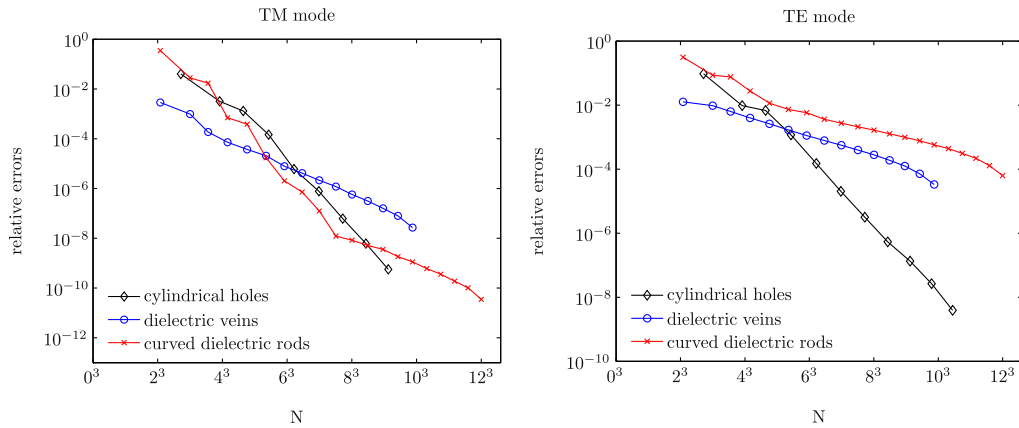


**Fig. 11.** The convergence of the relative error of the smallest TM (left) and TE eigenvalue (right) at  $k_c$  for the crystals with cylindrical holes, with dielectric veins and with inversely curved rods (Fig. 7, same geometric and dielectric parameters as in Figs. 8 and 9 (left)). The computations were done with  $p$ -FEM.

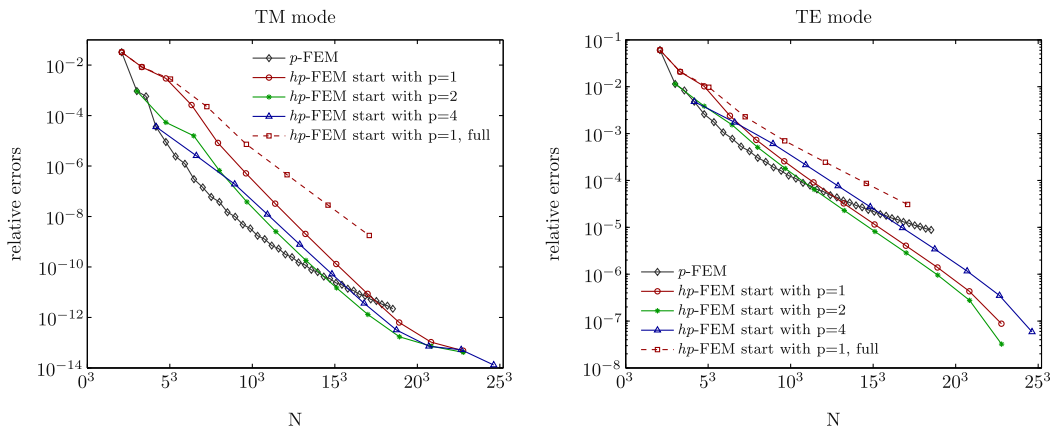


**Fig. 12.** Convergence of the relative error of the first eigenvalue at  $k_c$  for the TM-mode (left) and TE mode (right) of the crystal with dielectric veins ( $\varepsilon = 8.9$  in the veins,  $\varepsilon = 1$  in the middle, vein thickness 0.2 at each side). We use  $p$ -FEM and  $hp$ -FEM, the latter with different initial polynomial degree.

Although the band structure is shown for the symmetry lines of the reduced Brillouin zone only, the whole reduced Brillouin zone can be sampled conveniently, since the assembly of the matrices is done only once.

In addition to the eigenvalues the  $hp$ -adaptive FE algorithm also computes the eigenfunctions accurately. In Fig. 10, we see the squared amplitude<sup>8</sup> of the TM and the TE mode of the first band at the  $M$  point for the crystal with the perturbed  $9 \times 9$  dielectric vein structure (see Fig. 7).

We have chosen the geometric and dielectric parameters for the crystal with dielectric veins (Fig. 7) the same as in [12,13,24]. In [12,13] separation of variables approaches are applied, whereas in [24] first order FE are used. The comparison of these results to ours computed with  $p$ -FEM (see Table 1) validates our approach and our implementation. Notice the higher accuracy for the TM mode for the same refinement level due to weaker singularities at the interface corners. We present further convergence results in Section 4.2.

#### 4.2. Convergence of eigenvalues

Now, we investigate the convergence of the eigenvalues for different refinement strategies, starting with  $p$ -refinement. We choose the midpoint between  $\Gamma$  and  $X$ , which we name  $k_c$ . This is not a particularly “good” or “bad” one.

In Fig. 11 the convergence of the smallest eigenvalue is shown for the crystals with cylindrical holes, with dielectric veins and with inversely curved rods (Fig. 7) – for the TM and the TE mode, computed with  $p$ -FEM. For the cylindrical holes with only smooth material interfaces we observe exponential convergence in the number of degrees of freedom  $N$  as  $\exp(-\beta N^{1/3})$  as we expected from  $hp$ -theory [31,32,19]. For the crystals with dielectric veins and with inversely curved rods corner interfaces are present and the slope is less steep than for the crystal with cylindrical holes. Due to the smaller inward angle of the dielectric medium at the interface corners the singularity for the inversely curved rods is larger than for the dielectric veins [29], such that we observe a weaker convergence of the eigenvalues.

In Fig. 11 the eigenvalues of the crystal with the dielectric veins and the inversely curved rods seem to converge exponentially for  $p$ -FEM, although interface corners are present. Nevertheless, if we continue with the  $p$  refinement (in Fig. 12 for dielectric veins up to  $p = 38$ ), merely algebraic convergence emerges<sup>9</sup>.

In the following we investigate the convergence of the eigenvalues for geometric refinement – described in Section 2.5 – in comparison to  $p$ -FEM. In Fig. 12 the relative error of the smallest eigenvalue for the crystal with dielectric veins (Fig. 7) with thickness  $0.4a$  and  $\varepsilon = 8.9$  is shown. Starting with a coarse mesh with nine cells and  $p = 1$  in all cells,  $hp$ -FEM shows exponential convergence in contrast to  $p$ -FEM, both for the TE and the TM mode. However, in the beginning the polynomial refinement performs better

<sup>8</sup> The squared amplitude corresponds to the concept of probability density in quantum electrodynamics.

<sup>9</sup> With large convergence rate.

**Table 2**

Convergence of the first eigenvalue for the TE mode for the crystal with dielectric veins (see Fig. 7,  $\varepsilon = 8.9$ , vein thickness 0.2 at each side) at  $k = (1/2a, 0)$  for pure mesh refinement ( $h$ -FEM), pure polynomial order enlargement ( $p$ -FEM) and adaptive  $hp$ -FEM

Level	$h$ -FEM		$p$ -FEM		$hp$ -FEM	
	#Dof	$\frac{\omega_{TE,0}a}{2\pi c}$	#Dof	$\frac{\omega_{TE,0}a}{2\pi c}$	# Dof	$\frac{\omega_{TE,0}a}{2\pi c}$
1	9	0.521302619112	9	0.521302619112	9	0.521302619112
2	36	0.501735291198	27	0.497095810781	27	0.497095810781
3	144	0.494952283861	45	0.495570239622	108	0.493365508380
4	576	0.492664756896	72	0.493837964737	268	0.492231220419
5	2304	0.491885702189	108	0.492751880410	512	0.491725406461
6	9216	0.491618020101	153	0.492340949399	904	0.491563775139
7			207	0.491998065356	1492	0.491506786403
8			270	0.491855851430	2324	0.491486485296
9			342	0.491735848233	3448	0.491479231178
10			423	0.491681227299	4912	0.491476634000
11			513	0.491624540578	6764	0.491475702552
12			612	0.491597555930	9052	0.491475368251
13			720	0.491568698587	11824	0.491475248235
14			837	0.491554083965		
15			963	0.491537578751		
18			1395	0.491513511149		
23			2295	0.491493587640		
28			3420	0.491485836966		
33			4770	0.491481669113		
38			6345	0.491479554612		

For  $p$ -FEM and  $hp$ -FEM the level corresponds to the maximal polynomial degree in the discrete space. With  $hp$ -FEM we first refine only the polynomial degree and start then with geometric mesh refinement towards the four interface corners. With extrapolation (exponential ansatz) we expect  $\omega_{TE,0}a/2\pi c \approx 0.4914752$ .

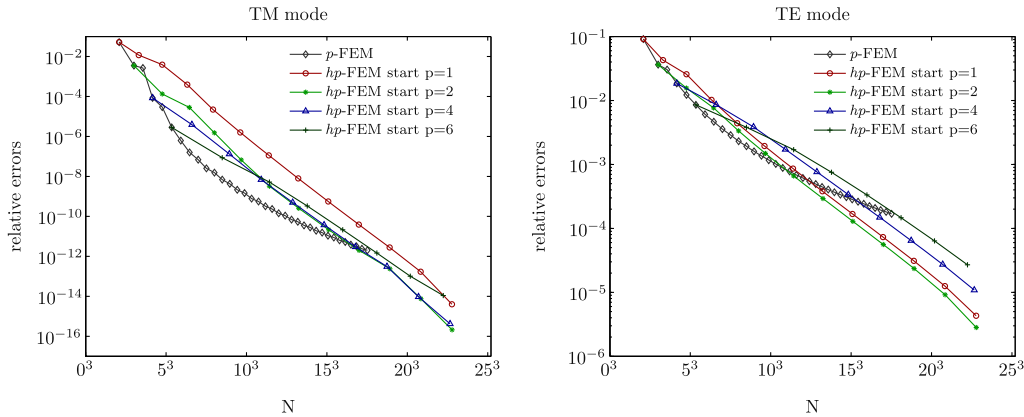


**Fig. 13.** Convergence of the relative error of the first eigenvalue at  $k_c$  for the TM-mode (left) and TE mode (right) of the crystal with curved dielectric veins (the third crystal in Fig. 7). We use  $\varepsilon = 100$  in the white region and  $\varepsilon = 1$  in the rest. The distance between the corners is  $0.6a$ , the circles used for the veins have radius  $0.8a$ , their midpoints lie on the perpendicular bisectors of the sides. We use  $p$ -FEM and  $hp$ -FEM, the latter with different initial polynomial degree.

(up to  $N \sim 4000$  for the TM mode, up to  $N \sim 2000$  for the TE mode). Therefore, we investigated the influence of the polynomial order in the coarse mesh for  $hp$ -FEM. The results in Fig. 12 show, that an initial polynomial order of  $p = 2$  performs better than one of order  $p = 1$  for all  $N$ , and that  $p = 4$  performs even better in the beginning, but converges with flatter slope. This behaviour is due to the weak singularities for the used material parameters. Note that the strategy reduces the relative error at about  $N = 8000$  for the TM mode to the order of  $10^{-14}$ , but for the TE mode only to the order of  $10^{-6}$ . In Fig. 12 we additionally show the relative error using full tensor-product spaces. Clearly the slopes of these curves for TE and TM mode are not as steep as the ones using trunk spaces. Both methods show exponential convergence as in (12), however with full tensor-product spaces the constant  $\beta$  is worse.

Table 2 shows the numerical TE eigenvalues for the setting just described (as in the left diagram in Fig. 12) for  $hp$ -FEM with initial polynomial order<sup>10</sup>  $p = 2$ , for  $p$ -FEM, and pure  $h$ -refinement ( $p = 1$ ).  $h$ -FEM also converges algebraically, but more slowly than  $p$ -FEM. At

$h$ -FEM-level 6 ( $N = 9216$ ) only three digits of the eigenvalue are exact, while with  $p$ -FEM at  $N = 6345$  five digits are exact and with the described  $hp$ -FEM-strategy at  $N = 6764$  (level 11) there are already six exact digits. With extrapolation of the  $hp$ -FEM-values we get 0.4914752, which we take for exact up to seven digits (one more).

Finally, we analyse the convergence behaviour for a crystal with curved dielectric veins (the third crystal in Fig. 7), where we even choose an artificially high dielectric contrast (100:1), to have an example with a very strong singularity in the TE mode. We choose  $\varepsilon = 100$  in the dark region of Fig. 7 and  $\varepsilon = 1$  in the rest of the structure. The distance between the corners is  $0.6a$ , the curvature is determined by circles with radius  $0.8a$  and midpoints on the perpendicular bisectors of the sides. The results of the computations with the same refinement strategies as in the previous example (see Fig. 12) are shown in Fig. 13. For the TE mode the convergence is much slower and  $hp$ -FEM clearly beats polynomial refinement, already at an accuracy of  $10^{-3}$ . Note that in Fig. 13 we have a relative error of  $10^{-5}$  (TE) at  $N = 8000$  in comparison to  $10^{-7}$  in Fig. 12. The worse convergence in the TE mode points to the stronger singularity due to the increased contrast and the outer angle

<sup>10</sup> More exactly, geometric refinement starts after a first  $p$ -refinement step.

which is larger due to the curved edges. The polynomial refinement for the TM mode is most efficient up to a relative error bound around  $10^{-12}$ , then *hp*-FEM with initial polynomial degrees of 2 and 4 takes over.

## 5. Conclusion

We introduced an algorithm based on *hp* finite elements with hanging nodes for computing the photonic crystal band structure. We showed that the eigenvalues converge exponentially for smooth and polygonal interfaces. In examples with polygonal interfaces we observed faster convergence with pure polynomial enrichment (*p*-FEM) for the first refinement levels than with *hp*-FEM – both for the TM and the TE mode. This is due to the relatively weak singularities. Nevertheless to achieve very high accuracies, *hp*-FEM is by far more efficient than *p*-FEM, especially when the singularities are stronger. The discretisation error of pure cell refinement (*h*-FEM) shows much slower convergence. These results meet the expectations from *hp*-FEM theory.

The presented algorithm is able to compute the band structure for polygonally shaped elementary cells to high accuracy at low computational costs. This is due to the exponential convergence of *hp*-FEM and because the system matrices are assembled only once for the whole Brillouin zone.

To extend the idea of the presented algorithm to 3D photonic crystals one could use *hp*-adaptive nodal elements with weighted regularisation [39] or *hp*-adaptive edge elements [40,20].

## Acknowledgements

The authors would like to thank Prof. R. Hiptmair, Prof. Ch. Schwab (both ETH Zürich, Switzerland) and Prof. M. Dauge (Université de Rennes 1, France) for their support and assistance.

## References

- [1] J.D. Joannopoulos, R.D. Meade, J.N. Winn, *Photon. Cryst.: Molding Flow Light* (1995).
- [2] Eli Yablonovitch, Inhibited spontaneous emission in solid-state physics and electronics, *Phys. Rev. Lett.* 58 (20) (1987) 2059–2062.
- [3] Peter Kuchment, *Floquet Theory for Partial Differential Equations*, Birkhäuser Verlag, Basel, 1993.
- [4] K. Busch, Photonic band structure theory: assessment and perspectives, *Compte Rendus Phys.* 3 (53) (2002) 53–66.
- [5] Robert D. Meade, Karl D. Brommer, Andrew M. Rappe, J.D. Joannopoulos, Existence of a photonic band gap in two dimensions, *Appl. Phys. Lett.* 61 (4) (1992) 495–497.
- [6] R.D. Meade, A.M. Rappe, K.D. Brommer, J.D. Joannopoulos, O.L. Alerhand, Accurate theoretical-analysis of photonic band-gap materials, *Phys. Rev. B* 48 (11) (1993) 8434–8437.
- [7] Steven G. Johnson, J.D. Joannopoulos, Block-iterative frequency-domain methods for maxwell's equations in a planewave basis, *Optics Express* 8 (3) (2001) 173–190.
- [8] K.M. Leung, Y. Qiu, Multiple-scattering calculation of the two-dimensional photonic band structure, *Phys. Rev. B* 48 (11) (1993) 7767–7771.
- [9] Kazuo Ohtaka, Tsuyoshi Ueta, Katsuki Amemiya, Calculation of photonic bands using vector cylindrical waves and reflectivity of light for an array of dielectric rods, *Phys. Rev. B* 57 (4) (1998) 2550–2568.
- [10] W.C. Saylor, F.M. Mueller, Pierre R. Villeneuve, Augmented-plane-wave method for photonic bandgap materials, *Phys. Rev. B* 57 (15) (1998) 8819–8822.
- [11] Esteban Moreno, Daniel Erni, Christian Hafner, Band structure computations of metallic photonic crystals with the multiple multipole method, *Phys. Rev. B* 65 (15) (2002) 155120.
- [12] Alexander Figotin, Yuri A. Godin, The computation of spectra of some 2D photonic crystals, *J. Comput. Phys.* 136 (1997) 585–598.
- [13] Igor Ponomarev, Separation of variables in the computation of spectra in 2-D photonic crystals, *SIAM J. Appl. Math.* 61 (4) (2001) 1202–1218.
- [14] J.B. Pendry, A. MacKinnon, Calculation of photon dispersion relations, *Phys. Rev. Lett.* 69 (19) (1992) 2772–2775.
- [15] C.T. Chan, Q.L. Yu, K.M. Ho, Order-*n* spectral method for electromagnetic waves, *Phys. Rev. B* 51 (23) (1995) 16635–16642.
- [16] Kazuaki Sakoda, Jun Kawamata, Novel approach to photonic bands with frequency-dependent dielectric constants, *Optics Express* 3 (1) (1998) 12–18.
- [17] Dietrich Braess, *Finite Element*, Springer, Berlin, 2003.
- [18] Barna Szabo, Ivo Babuska, *Finite Element Analysis*, John Wiley & Sons, New York, 1991.
- [19] Christoph Schwab, *p- and hp- Finite Element Methods: Theory and Applications in Solid and Fluid Mechanics*, Oxford University Press, 1998.
- [20] Leszek Demkowicz, *Computing with HP-Adaptive Finite Elements: One and Two Dimensional Elliptic and Maxwell Problems*, Chapman and Hall/CRC Applied Mathematics and Nonlinear Science, 2006.
- [21] I. Babuska, B.Q. Guo, The *h-p* version of the finite element method for domains with curved boundaries, *SIAM Numer. Anal.* 25 (1988) 837–861.
- [22] M. Ainsworth, B. Senior, An adaptive refinement strategy for *hp*-finite element computations, *Appl. Numer. Math.* 26 (1998) 165–178.
- [23] W. Dörfler, V. Heuveline, Convergence of an adaptive *hp* finite element strategy in one space dimension, *Appl. Numer. Math.* 57 (10) (2007) 1108–1124.
- [24] Waldemar Axmann, Peter Kuchment, An efficient finite element method for computing spectra of photonic and acoustic band-gap materials i. Scalar case, *J. Comput. Phys.* 150 (1999) 468–481.
- [25] David C. Dobson, An efficient method for band structure calculations in 2D photonic crystals, *J. Comput. Phys.* 149 (2) (1999) 363–376.
- [26] David C. Dobson, Jayadeep Gopalakrishnan, Joseph E. Pasciak, An efficient method for band structure calculations in 3D photonic crystals, *J. Comput. Phys.* 161 (2) (2000) 668–679.
- [27] Daniele Boffi, Matteo Conforti, Lucia Gastaldi, Modified edge finite elements for photonic crystals, *Numer. Math.* 105 (2) (2006) 249–266.
- [28] Charles Kittel, *Introduction to Solid State Physics*, John Wiley & Sons, New York, 2004.
- [29] Martin Petzold, Regularity and error estimates for elliptic problems with discontinuous coefficients, PhD thesis, FU Berlin, Berlin, January 2001.
- [30] M. Costabel, M. Dauge, S. Nicaise, Singularities of Maxwell interface problems, *Rairo-Math. Model. Numer. Anal.-Model. Math. Et Anal. Numer.* 33 (3) (1999) 627–649.
- [31] I. Babuska, B.Q. Guo, J.E. Osborn, Regularity and numerical solution of eigenvalue problems with piecewise analytic data, *SIAM J. Numer. Anal.* 26 (6) (1989) 1534–1560.
- [32] Ben Qi Guo, Hae Soo Oh, The *h-p* version of the finite element method for problems with interfaces, *Int. J. Numer. Methods Engrg.* 37 (10) (1994) 1741–1762.
- [33] George Em Karniadakis, Spencer J. Sherwin, *Spectral/hp Element Methods for Computational Fluid Dynamics*, Oxford University Press, Oxford, 1999.
- [34] Philipp Frauenfelder, *hp*-finite element methods on anisotropically, locally refined meshes in three dimensions with stochastic data, PhD thesis, ETH Zürich, Zürich, 2004.
- [35] Philipp Frauenfelder, Christian Lage, Concepts – an object-oriented software package for partial differential equations, *Math. Model. Numer. Anal.* 36 (5) (2002) 937–951.
- [36] Concepts Development Team. Concepts homepage, 2008. <<http://www.concepts.math.ethz.ch>>.
- [37] R.B. Lehoucq, D.C. Sorensen, P.A. Vu, C. Yang, Arpack: fortran subroutines for solving large scale eigenvalue problems.
- [38] James W. Demmel, Stanley C. Eisenstat, John R. Gilbert, Xiaoye S. Li, Joseph W.H. Liu, A supernodal approach to sparse partial pivoting, *SIAM J. Matrix Anal. Appl.* 20 (3) (1999) 720–755.
- [39] Martin Costabel, Monique Dauge, Christoph Schwab, Exponential convergence of *hp*-FEM for Maxwell's equations with weighted regularization in polygonal domains, *Math. Model. Methods Appl. Sci.* 15 (4) (2005) 575–622.
- [40] Mark Ainsworth, Joe Coyle, Paul D. Ledger, Ken Morgan, Computing Maxwell eigenvalues by using higher order edge elements in three dimensions, *IEEE Trans. Magn.* 39 (5) (2003) 2149–2153.